Journal of Materials Chemistry A

ROYAL SOCIETY OF CHEMISTRY

PAPER

View Article Online
View Journal | View Issue



Cite this: J. Mater. Chem. A, 2025, 13, 42204

# Decoding host–guest interactions: tuning pore functionality in MOFs for efficient capture of short- and long-chain PFAS

Lidia García,†[a] Patricia García-Atienza, †[b] Sergio Armenta, [b] José Manuel Herrero-Martínez, *[b] Mario Prejanò, [c] Tiziana Marino, [c] Donatella Armentano, *[c] Thais Grancha, [a] Jesús Ferrando-Soria [a] and Emilio Pardo *[a]

Per- and polyfluoroalkyl substances (PFAS) are persistent environmental pollutants of growing concern due to their widespread occurrence, chemical stability, and adverse health effects. In this study, we explore the impact of pore-surface functionality in a series of bio-derived metal–organic frameworks (MOFs), including multivariate MOFs (MTV-MOFs), as a strategy for designing next-generation adsorbents for the efficient removal of both long- and short-chain PFAS from aqueous solutions. Building on a previously reported MOF featuring thioether-functionalized channels (MOF **1**), we synthesized and evaluated four structural analogues (MOFs **2**–**5**), systematically tuning pore chemistry through amino acid side-chain substitutions (L-serine and L-leucine). Adsorption studies reveal that increasing the hydrophobicity of the pore environment significantly enhances PFAS uptake, particularly for short-chain compounds. MOF **5**, incorporating L-leucine-based hydrophobic side chains, demonstrated superior performance across all tested PFAS, along with excellent reusability and high sorption capacity. Single-crystal X-ray diffraction provided molecular-level insight into host–guest interactions, confirming both metal coordination and key supramolecular interactions. Complementary theoretical calculations based on the resolved crystal structure of MOF **5** with embedded PFOA molecules (**PFOA@5′**) further confirm the dominant role of rationally introduced hydrophobic functionalities in driving efficient PFAS capture. These findings underscore the central role of pore functionality in enabling efficient, tuneable MOF platforms for water remediation.

Received 15th September 2025
Accepted 11th November 2025

DOI: 10.1039/d5ta07539d

rsc.li/materials-a



## 1. Introduction

Per- and polyfluoroalkyl substances (PFAS)[1,2] are synthetic chemicals renowned for their exceptional durability and resistance to degradation.[3,4] Widely used for decades in non-stick cookware, waterproof textiles, firefighting foams, and even lithium-ion battery components,[5,6] their chemical stability ensures functionality but also environmental persistence. PFAS now contaminate water, soil, and biota worldwide,[7–9] and exposure has been linked to cancer, immune suppression, and developmental disorders.[10] Their persistence and toxicity have triggered increasingly strict regulations,[11] such as the recent European directive limiting total PFAS in discharged water to 0.5 ppb,[12] a threshold that existing treatment technologies rarely meet.

Eliminating PFAS remains an enormous challenge[13] because of their amphiphilic molecular architecture – hydrophobic, fluorinated tails coupled with hydrophilic headgroups – that limits reactivity and complicates degradation. Advanced oxidation, electrochemical, and thermal treatments can break down PFAS but generally require high energy inputs and specialized conditions that restrict scalability.[14] Adsorption-based approaches therefore remain among the most practical options for PFAS removal. Within them, some remarkable adsorption platforms are biochars,[15] ion-exchange resins,[16] high-pressure membranes[17] and activated carbons.[18–20] However, while they offer significant benefits, they are not without limitations. For example, granular activated carbon (GAC)[21] exhibits typical adsorption capacities exceeding ~200 mg $g^{-1}$ for long-chain PFOS or PFOA, but fall below ~30 mg $g^{-1}$ for short-chain PFAS,[22] such as PFBA or PFHxA. A similar trend is observed for removal efficiencies – GAC can remove >90% of long-chain PFAS under favourable conditions, yet only <30–50% of short-chain PFAS unless powdered

[a]Instituto de Ciencia Molecular (ICMol), Universidad de Valencia, 46980 Paterna, Valencia, Spain. E-mail: emilio.pardo@uv.es

[b]Departamento de Química Analítica, Universitat de València, c/Dr Moliner, 50, 46100 Burjassot, Valencia, Spain. E-mail: Jose.M.Herrero@uv.es

[c]Dipartimento di Chimica e Tecnologie Chimiche (CTC), Università della Calabria, Rende 87036, Cosenza, Italy. E-mail: Donatella.armentano@unical.it

† These authors have equally contributed to this work.

activated carbon (PAC) doses are increased dramatically (*e.g.*, 100–700 mg $L^{-1}$ required for 50% removal of $C_4$-PFCA).[23] In addition, competitive adsorption from co-contaminants and slow regeneration rates diminish efficiency and raise operating costs. Thus, these challenges highlight the need for new, high-capacity, and reusable adsorbents capable of capturing both long- and short-chain PFAS.

Metal–organic frameworks (MOFs)[24–26] have emerged as a particularly promising class of porous adsorbents owing to their exceptionally high surface areas, tuneable pore sizes, and chemically tailorable internal functionalities.[27] Their modular design enables precise control over pore chemistry,[28] offering opportunities to optimize interactions with PFAS molecules through hydrophobic, electrostatic, and hydrogen-bonding effects. Multivariate MOFs (MTV-MOFs),[29] in particular, permit the introduction of diverse functional groups within a single framework,[30] thus fine-tuning adsorption sites without compromising structural integrity. Originally explored for gas storage,[31] catalysis[32–34] or drug delivery,[35] MOFs have recently demonstrated potential in water purification and pollutant capture.[36,37]

Their structural versatility makes MOFs particularly well-suited for PFAS removal.[38] Unlike other adsorbents, MOFs offer precise control over pore dimensions and surface functionalities,[39,40] enabling *a priori* selective adsorption of both long- and short-chain PFAS. By tailoring the functional groups within their pores, these materials can enhance PFAS affinity, resulting in more efficient and rapid removal. However, despite their extraordinary properties and immense promise as PFAS adsorbents,[38,41,42] relatively few studies have demonstrated the effectiveness of MOFs in PFAS capture.[43–60] Moreover, most studies have focused exclusively on long-chain PFAS,[43–60] whereas only a handful have examined short-chain analogues, typically reporting limited removal efficiencies.[45,60] For example, some MOFs have achieved over 90% removal efficiencies for PFOA and PFOS under laboratory conditions,[61] while their performance against short-chain PFAS remains more modest (<20–40% for UiO-66 variants).[56] This disparity underscores the importance of understanding the molecular interactions governing PFAS–MOF affinity. The higher hydrophilicity of shorter PFAS chains reduces their affinity for MOF surfaces, making them more difficult to capture. Overall, advancing PFAS remediation requires systematic studies to elucidate adsorption mechanisms and structure–property relationships in MOFs, which could ultimately lead to a deeper understanding of PFAS–MOF interactions. Expanding research in this area may unlock powerful strategies for designing frameworks capable of addressing one of the most persistent environmental challenges of our time.

## 2. Results and discussion

In this work, we aim to advance the understanding of the interactions that govern the PFAS capture process by MOFs, with the ultimate goal of designing increasingly efficient materials. To achieve this, we took as a starting point a previously reported MOF – with formula $\{Ca^{II}Cu^{II}_6[(S,S)\text{-methox}]_3(OH)_2(H_2O)\}\cdot 16H_2O$ (**1**)[62] (Fig. 1 and Scheme S1), where methox is the oxamidato-based ligand bis[(*S*)-methionine]oxalyl diamide) – with outstanding performances in water remediation. In particular, MOF **1** had previously demonstrated high efficiency in capturing heavy metals[63–65] and organic pollutants such as insecticides,[66] antibiotics[67] or organic dyes.[30,68] The reasons behind these exceptional capture properties are diverse. Firstly, **1** features medium-sized hexagonal channels (*ca.* 1 nm) densely decorated with thioether residues ($-CH_2CH_2SCH_3$), which have been shown to establish weak supramolecular interactions with guest molecules, including hydrophobic interactions and the often underestimated sigma–hole interactions.[68,69] Additionally, the $-CH_2CH_2SCH_3$ "arms" exhibit remarkable flexibility and adaptability,[70] allowing them to adjust and accommodate guest molecules by maximizing the aforementioned host-guest interactions. Finally, MOF **1** possesses accessible unsaturated copper(II) centres which are susceptible to coordination by the carboxylate or sulfonate groups from PFAS (Scheme S2).

The initial objective, therefore, was to evaluate the efficacy of MOF **1** in capturing a series of selected PFAS. Subsequently, we aimed to assess the role played by the amino acid residues decorating the pores in this capture process. To achieve this, we took advantage of the ability of this MOF family (including MTV-MOFs) to produce isoreticular MOFs that maintain the same architecture while modifying only the side chains within the pores (Fig. 1 and Scheme S1). Thus, we introduced greater hydrophilicity into MOF **1** after replacing 50% of the thioether residues with serine residues ($-CH_2OH$) by synthesizing MTV-MOF **2**,[30] with the formula $\{Ca^{II}Cu^{II}_6[(S,S)\text{-methox}]_{1.5}[(S,S)\text{-serimox}]_{1.5}(OH)_2(H_2O)\}\cdot 30H_2O$. Additionally, we can also obtain MOF **3**, with the formula $\{Ca^{II}Cu^{II}_6[(S,S)\text{-serimox}]_3(OH)_2(H_2O)\}\cdot 39H_2O$ and with (*S*,*S*)-serimox being bis[(*L*)-serine]oxalyl diamide,[71] in which 100% of the side chains decorating the channels originate from the amino acid L-serine. Conversely, the hydrophobicity of the channels in MOF **1** can be increased by synthesizing another MTV-MOF, MOF **4**, with the formula $\{Ca^{II}Cu^{II}_6[(S,S)\text{-methox}]_{1.5}(S,S)\text{-leumox}]_{1.5}(OH)_2(H_2O)\}\cdot 17H_2O$, which retains 50% of the thioether residues while introducing 50% of side chains ($-CH_2CH(CH_3)_2$) from the amino acid L-leucine. The obvious final step is to synthesize MOF **5**, with formula $\{Ca^{II}Cu^{II}_6[(S,S)\text{-leumox}]_3(OH)_2(H_2O)\}\cdot 11H_2O$ with (*S*,*S*)-leumox being bis[(L)-leucine]oxalyl diamide,[72] in which 100% of the side chains decorating the pores consist of ($-CH_2CH(CH_3)_2$).

This family of MOFs and MTV-MOFs (**1–5**), as a whole, provides a suitable playground for evaluating the influence of hydrophilicity/hydrophobicity and the corresponding host-guest interactions in the PFAS capture process. Remarkably, the extraordinary crystallinity of this family of MOFs also allows, by single-crystal X-ray diffraction (SCXRD), to resolve the crystal structures of some host-guest adsorbates allowing thus an unprecedented structural visualization on PFAS interactions with the framework as well as on the molecular recognition process involved in the capture process. Moreover, theoretical calculations carried out on resolved crystal structures of host-guest adsorbates should undoubtedly shed light on the dominant interactions established between the functional channels of the MOF and the target PFAS. Finally, the ultimate goal is

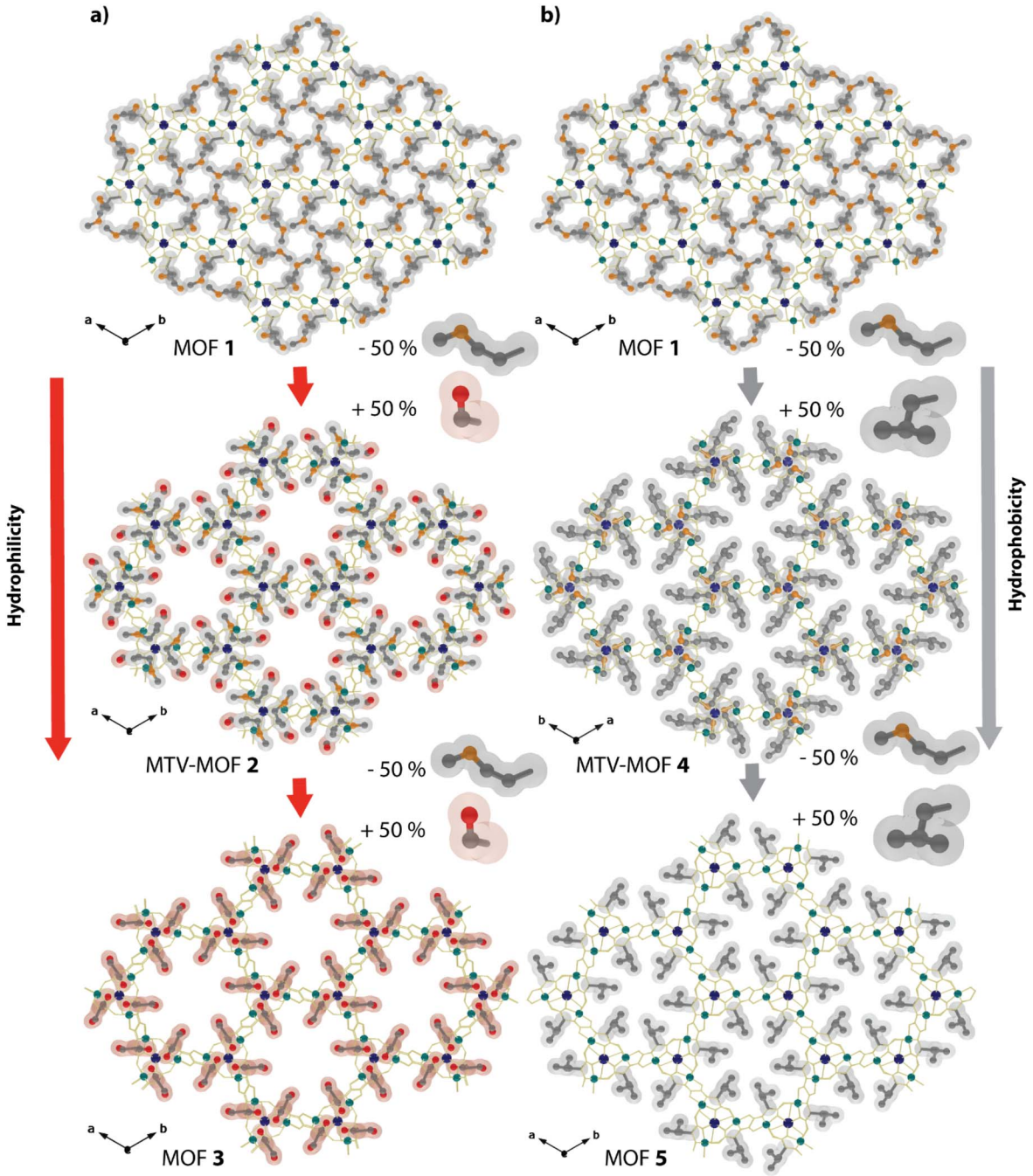


Fig. 1 Perspective view along the crystallographic *c* axis of the porous structures of **1** (a top and b top), **2** (a centre), **3** (a bottom), **4** (b centre) and **5** (b bottom) highlighting the dual route aiming at increasing hydrophilicity (a) and hydrophobicity (b). The copper(II) and calcium(II) cations are represented by cyan and blue spheres, respectively, whereas organic ligands (except side chains from amino acids) forming the network are represented by yellow sticks. $-CH_2CH_2SCH_3$, $-CH_2OH$ and $-CH_2CH(CH_3)_2$ side chains from L-methionine, L-serine and L-leucine amino acids, respectively, are represented with spheres and thick sticks. Moreover, red and grey surfaces are used to highlight the hydrophilicity and hydrophobicity, respectively, of these residues.

undoubtedly to achieve the efficient capture of short-chain PFAS ($C_4$–$C_6$), which pose a significant challenge for modern societies.

### 2.1 Synthesis and characterization

Prior to exploring the capture properties, MOFs **1–3** and **5** were synthesized and characterized on a multigram scale, as previously reported.[30,62,71,72] These MOFs were obtained by direct precipitation in water. MOF **4**, reported herein for the first time, was synthesized following the same synthetic process (see Experimental section). In parallel, single crystals of MTV-MOF **4** and MOF **5**, suitable for single-crystal X-ray diffraction, were obtained using a slow diffusion method (see Experimental section).

 

As previously provided for **1–3** and **5** MOFs,[30,62,71,72] the crystal structure of MOF **4** was determined by SCXRD (Table S1). MOF **4** results isoreticular to MOFs **1–3** and **5** and crystallizes in the chiral $P6_3$ space group. Its structure consists of a six-connected 3D calcium(II)-copper(II) network, described by an acs underlying net, featuring hexagonal channels with diameter pore sizes of approximately 0.6 nm (Fig. 1 and S1–S4). Within these pores, adaptable amino acid residues – the ethylenethiomethyl ($-CH_2CH_2SCH_3$) from L-methionine and the 2-methylpropyl ($-CH_2CH(CH_3)_2$) from L-leucine – coexist in a 1 : 1 ratio (refer to colour code in Fig. 1). The crystal structure confirms the expected confinement of these amino acid functionalities, which in turn imparts flexibility to the pores. This flexibility allows each amino acid chain to stabilize its conformation based on the target guest molecules (see crystal structures of host-guest aggregates below). In detail, while the isobutyl (2-methylpropyl) residue exhibits a distended conformation inwards the pores, the ethylenethiomethyl from L-methionine adopts a highly bent conformation with their methyl groups pointing outward the pores (Fig. S1 and S2). L-Leucine residues, being more hydrophobic and longer and so more hindered than others, most likely prefer to be buried in large space to reach the more stable folding. For understanding the structure–properties relationship, it is important to highlight that the significant flexibility is only confined within channels of the framework, and observed for both the longer isobutyl side chain of L-leucine and the L-methionine residue, will undoubtedly influence capture performance within the pores. Therefore, this flexibility is a crucial synergistic factor to consider when aiming for precise control over selectivity. Notably, the X-ray structure reveals high thermal motion of the carbon atoms belonging to the L-leucine amino acid residues in **4**. This suggests the possibility of further optimizing the conformation of these sidechains, which could enhance efficient host-guest interactions with PFAS as target molecules (Fig. S2–S4).

The experimental powder X-ray diffraction (PXRD) patterns of MOFs **1–5** are shown in Fig. S5 and S6. They confirm the purity and homogeneity of the bulk samples, as they are consistent with the theoretical patterns. The homogeneity and morphological consistency of MOFs **1–5** were further corroborated by scanning electron microscopy (SEM). The SEM images of MOFs **1–5** (Fig. S7) exhibit comparable particle shapes and size distributions across all polycrystalline samples. The solvent content of the novel MOF **4** was estimated by thermogravimetric analysis (TGA) under dry $N_2$ atmosphere (see Fig. S8). Moreover, prior to carrying capture experiments, the permanent porosity of novel MOF **4** – and also that of previously reported MOFs **1–3** and **5**), was evaluated by measuring their $N_2$ adsorption isotherms (Fig. S9). These isotherms allowed to calculate the Brunauer–Emmett–Teller (BET) surface areas[73] for MOF **1** (108.3 $m^2\ g^{-1}$), MOF **2** (697.6 $m^2\ g^{-1}$), MOF **3** (903.3 $m^2\ g^{-1}$), MOF **4** (279.8 $m^2\ g^{-1}$) and MOF **5** (393.7 $m^2\ g^{-1}$). Additionally, to visualise the relative hydrophobicity/hydrophilicity within this family of MOFs, water contact angle measurements were carried out for MOFs **3** (L-serine), **1** (L-methionine) and **5** (L-leucine) (Fig. S10), which show a subtle increase in the contact angle as the hydrophobicity of the substituents decorating the pores increases (47.2°, 61.3° and 64.1°, respectively).

## 2.2 PFAS capture experiments

**2.2.1 Capture properties of MOFs 1–5.** The next step consisted on evaluating the goodness of MOFs **1–5** in PFAS removal. Thus, they were then used as solid-phase extraction (SPE) sorbents, towards a varied selection of representative long-chain ($\geq C_7$) PFAS like perfluoroheptanoic acid (PFHpA), perfluoroheptanesulfonic acid (PFHpS), perfluorooctanoic acid (PFOA), perfluorooctanesulfonic acid (PFOS), perfluorononanoic acid (PFNA), perfluorodecanoic acid (PFDA), perfluoroundecanoic acid (PFUnDA), perfluorododecanoic acid (PFDoDA), 4 : 2 fluorotelomer sulfonic acid (4–2 FTSA), 6 : 2 fluorotelomer sulfonic acid (6–2 FTSA), 8 : 2 fluorotelomer sulfonic acid (8–2 FTSA), 9-chlorohexadecafluoro-3-oxanone-1-sulfonic acid (9Cl-PF3ONS) and 11-chloroeicosafluoro-3-oxaundecane-1-sulfonic acid (11Cl-PF3UdS) and also the challenging short-chain ($C_4$–$C_6$) PFAS like perfluorobutanoic acid (PFBA), perfluorobutanesulfonic acid (PFBS), perfluoropentanesulfonic acid (PFPeS), perfluorohexanoic acid (PFHxA) and perfluorohexanesulfonic acid (PFHxS).

As a starting point, the removal performance of MOF **1** was evaluated. To achieve this, SPE devices were prepared by placing 25 mg of the MOF **1** between two frits inside 1 mL empty polypropylene cartridges. Capture experiments were conducted in triplicate using a commercial aqueous solution containing a mixture of the eighteen selected PFAS. The contaminated solution was passed through the SPE device, and the quantification of the removed PFAS was determined by injecting the percolated SPE fractions—filtered through a PTFE membrane with a 0.22 μm pore size—into an LC-MS system (see Experimental section, Fig. 2 and Table S2). The efficiency of MOF **1**, which features moderately hydrophobic thioether residues decorating its pores, is rather modest, as it is only capable of fully capturing long-chain PFAS ($C_8$), such as PFOS and PFDA, while exhibiting very poor retention for short-chain PFAS ($C_4$–$C_6$) (see Fig. 2). Overall, the performance of MOF **1** does not improve that previously reported[45] for the reference material, namely powder activated carbon (PAC) which has been measured with these experimental conditions for the sake of comparison.

At this point, we started evaluating the influence on the capture properties of replacing 50% of the L-methionine ($-CH_2CH_2SCH_3$) residues with L-serine ($-CH_2OH$) residues in MTV-MOF **2** or by replacing 100% of them in MOF **3**. The experimental procedure is identical to that described for MOF **1**. Initially, the idea of introducing polar functional groups ($-CH_2OH$) inside the pores seemed promising, as this would incorporate functional groups more likely to interact with the hydrophilic part of the corresponding PFAS, which could be particularly relevant for the capture of short-chain PFAS. However, in general, and with the exception of PFHxS capture, no significant improvement in capture properties was observed, and for some PFAS, the performance even worsened (Fig. 2 and Table S2).

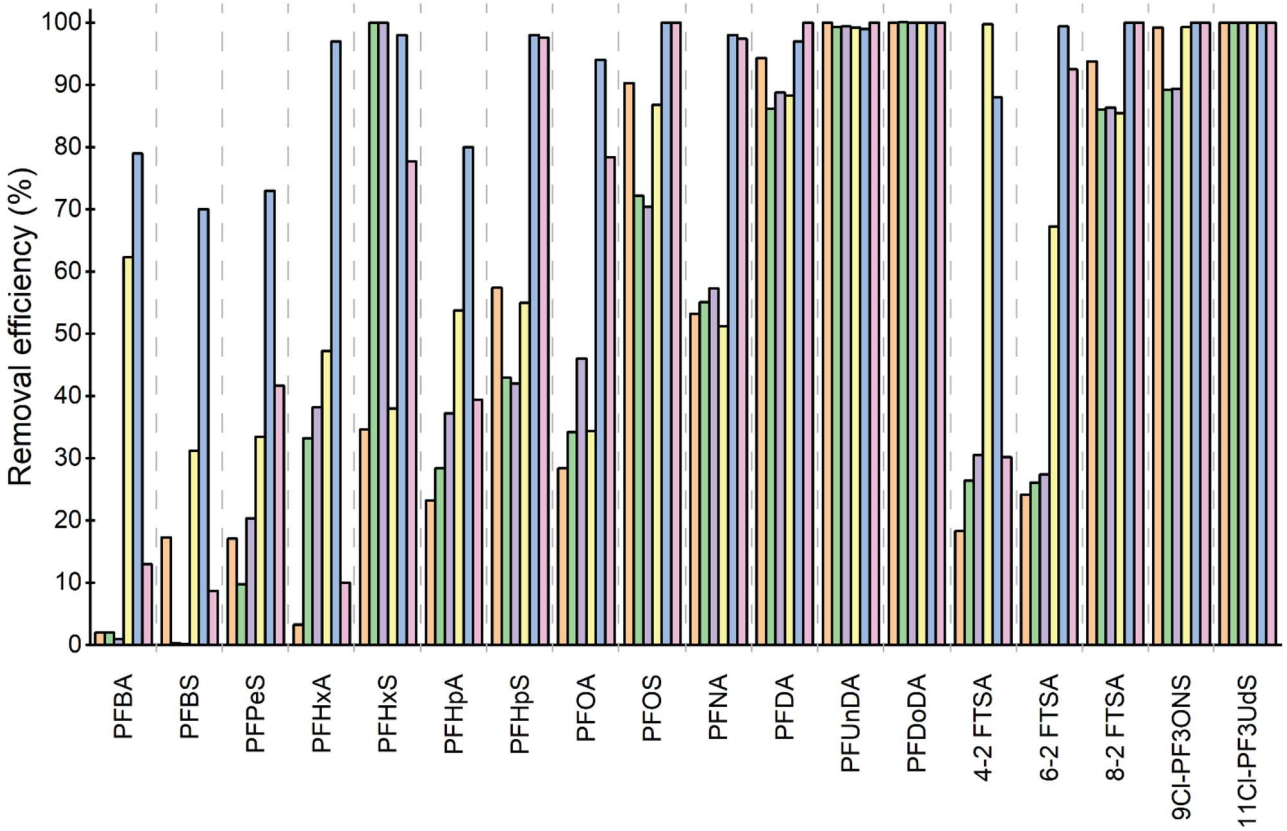


Fig. 2 Capture efficiency (%) of MOFs **1** (violet), **2** (green), **3** (orange), **4** (yellow), **5** (blue) and PAC (pink) from an aqueous solution containing a mixture of eighteen selected PFAS. Capture experiments were conducted in triplicate and the experimental data can be found in Table S2. Grey dashed lines are used to separate measurements for each PFAS.

Somewhat unexpectedly, the most remarkable results for short-chain PFAS were achieved by replacing 50% of the hydrophobic L-methionine residues with even more hydrophobic L-leucine ($-CH_2CH(CH_3)_2$) residues (MTV-MOF **4**), and especially by replacing 100% of them in MOF **5**, where all the side chains decorating the channels originate from L-leucine. Thus, a clear improvement in the capture properties of MTV-MOF **4** is observed compared to MOF **3** (Fig. 2 and Table S2), which is particularly relevant for the capture of short-chain PFAS. These results become truly remarkable for MOF **5**, which features 100% L-leucine side chains and achieves much improved efficiency for all analysed PFAS, both long-chain ($\geq C_7$) and short-chain ($C_4$–$C_6$). These findings make MOF **5** by far the most effective material for capturing this class of emerging contaminants, despite not exhibiting the highest BET surface area, thus highlighting the pre-eminent role of pore functionality in the capture process over simple surface area ("function-over-surface-area" design principle). These results complement a recent study on systematically functionalized porous polymer networks, where electrostatic interactions play a prevalent role, especially in combination with hydrogen fluorophilic ones, and the adsorbents with dominant hydrophobic interactions do not exhibit good performance for the removal of long-, and particularly, short-chain PFAS.[74]

**2.2.2 Kinetics.** This work (Section 2.2.1) extends beyond conventional kinetic frameworks typically applied under dispersive conditions, where extraction processes are primarily governed by equilibrium kinetics. To achieve a more comprehensive understanding, we also conducted kinetic analyses on two representative PFAS compounds, PFBA and PFOA. In these experiments, MOFs **4** and **5** were dispersed in aqueous solutions containing the respective PFAS, and the removal efficiency was monitored over time intervals ranging from 5 minutes to 2 hours. The experimental data were fitted to commonly used kinetic models, including the pseudo-first-order and pseudo-second-order equations, to elucidate the adsorption mechanisms and identify the rate-controlling steps. The kinetic parameters obtained from the linearized plots (Fig. S11) – such as the rate constants and calculated equilibrium adsorption capacities – are summarized in Tables S7 and S8. Notably, the adsorption capacities ($Q_e$) derived from the pseudo-second-order model closely match the corresponding experimental values, and the exceptionally high correlation coefficients ($R^2 \approx 1.0$) indicate that the adsorption process is governed by chemisorption between PFAS molecules and the binding sites of MOF **4** or MOF **5**.

**2.2.3 Reusability experiments.** To assess not only the effectiveness of the material but also its potential for real-world application, the reusability of the best-performing MOF (**5**) was

 

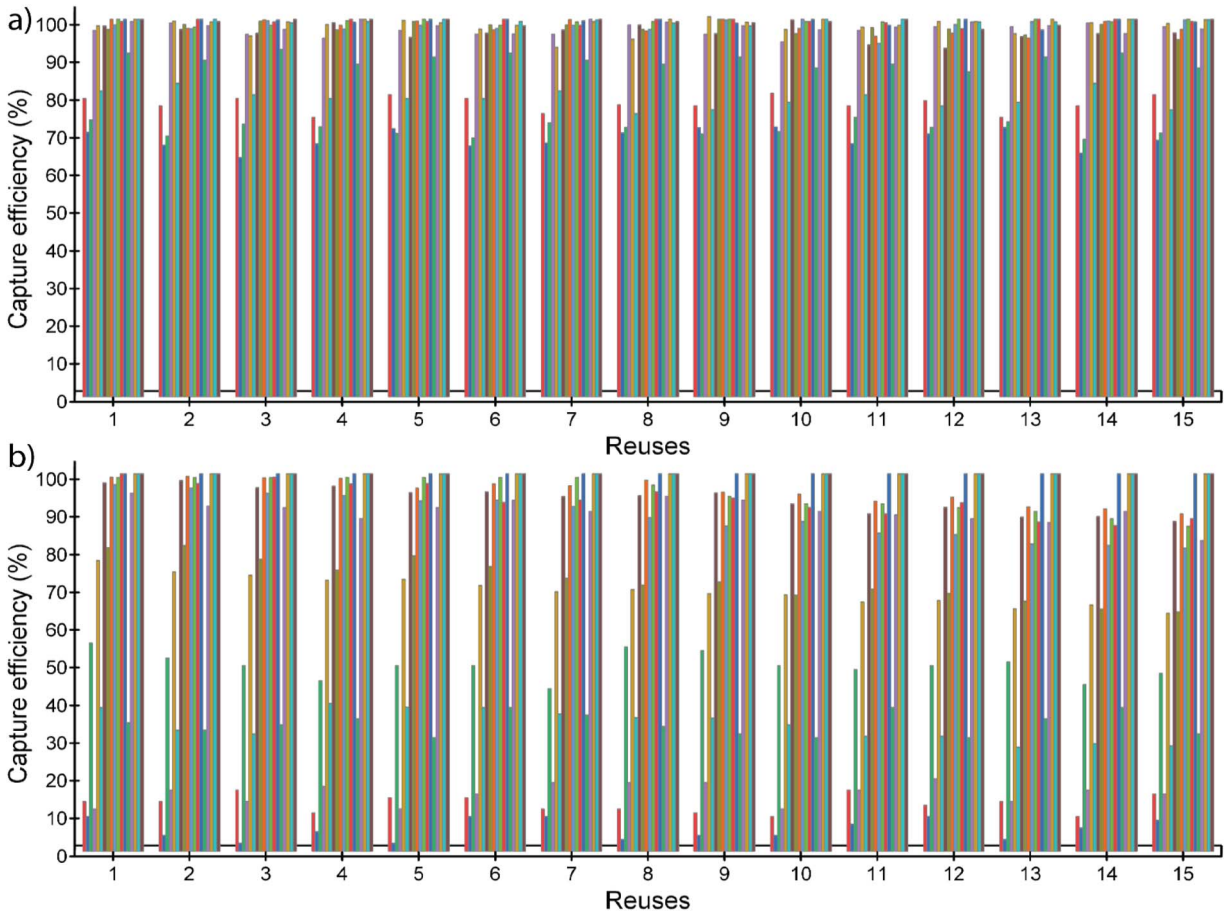


Fig. 3 Reuses of MOF **5** (a) and PAC (b) towards the mixture containing the different eighteen PFAS (from left to right: PFBA, PFBS, PFPeS, PFHxA, PFHxS, PFHpA, PFHpS, PFOA, PFOS, PFNA, PFDA, PFUnDA, PFDoDA, 4–2 FTSA, 6–2 FTSA, 8–2 FTSA, 9Cl-PF3ONS and 11Cl-PF3UdS). Capture experiments were conducted in triplicate and the experimental data can be found in Tables S3 and S4.

systematically evaluated. In order to better simulate real-world application scenarios – where regenerating the material after each decontamination cycle is often impractical – we conducted reuse experiments with 5 without applying full regeneration between cycles. Instead, only a small volume of eluent (5 mL of methanol) was passed through the system between measurements to remove residual analytes adsorbed on the surface of the MOF particles. Then, the capture efficiency of 5 was tested over 15 consecutive capture cycles using an aqueous solution containing 18 different PFAS (Fig. 3a and Table S3). Remarkably, MOF **5** maintained nearly the same high efficiency observed during the initial cycle (Fig. 2 and Table S2), demonstrating excellent stability and reusability. In contrast, powdered activated carbon (PAC), tested for comparison, exhibited a progressive decline in performance across cycles (Fig. 3b and Table S4). Furthermore, PXRD patterns of **5** after the 15-cycle reuse test confirmed that its crystalline structure remained intact (Fig. S12), underscoring its structural robustness under operational conditions.

**2.2.4 Maximum uptake capacity.** Aiming at investigating the maximum sorption capacities for these MOFs, we selected the best performing one, that is MOF **5**, and we carried out PFAS insertion experiments with four selected sulfonic acid-based PFAS. In so doing, polycrystalline samples of **5** (ref. 72) (50 mg) were soaked in saturated aqueous solutions of PFBS, PFPeS, PFHpS and PFOS for two weeks, replacing each saturated solution every 24 h. The maximum uptakes for PFBS, PFPeS, PFHpS and PFOS determined by C, H, S, N analyses, were 565, 598, 609 and 588 mg $g^{-1}$ respectively, which barely correspond to 3, 3, 2.5 and 2 PFAS molecules, respectively, per $Cu_6Ca$ unit (see SI for details). Fig. S13 shows the $N_2$ adsorption isotherms of **5+PFBS** (**PFBS@5**), **5+PFPeS** (**PFPeS@5**), **5+PFHpS** (**PFHpS@5**) and **5+PFOS** (**PFOS@5**), at 77 K. They exhibit very low adsorption values that are consistent with the enormous decrease in accessible void space in all these materials as their channels are occupied by guest molecules.

### 2.3 Crystal structures of host-guest adsorbates

Aiming at elucidating the mechanisms underpinning the exceptional PFAS capture efficiency of MOFs **4** and **5**, we conducted single-crystal X-ray diffraction (SCXRD) experiments on guest-loaded samples (Table S1). Initial attempts using single crystals of the primary Ca-MOFs (**4** and **5**) proved challenging. While these materials are effective for sorption, their single crystals did not maintain their integrity after only three days of being soaked in the guest solution.

To overcome this limitation and obtain the high-quality diffraction data essential for resolving the precise binding interactions, we employed a well-established strategy of using isoreticular $Cu_6Sr$ or $Cu_6Ba$ analogues, whose single crystals have previously been shown to better withstand the use of post-synthetic methods for encapsulating guest molecules.[66] Accordingly, we synthesized the Sr-based MOFs **4′** and **5′**, (with formulas $\{Sr^{II}Cu^{II}_6[(S,S)\text{-methox}]_{1.5}(S,S)\text{-leumox}]_{1.5}(OH)_2(H_2O)\}\cdot 17H_2O$ and $\{Sr^{II}Cu^{II}_6[(S,S)\text{-leumox}]_3(OH)_2(H_2O)\}\cdot 11H_2O$), which are isoreticular to **4** and **5**, as confirmed by SCXRD (Fig. 4 and S14–S18) and PXRD (Fig. S5, S6, S19 and S20) analyses, and exhibit identical capture properties. These Sr-analogues demonstrated superior structural integrity, retaining their crystallinity for over a week under identical soaking conditions. This enhanced stability was critical for acquiring a high-resolution crystallographic dataset. It is important to note that the host-guest interactions observed in these Sr-analogues are considered fully transferable to explain the performance of the original Ca-MOFs. The sorption process is driven by the chemical functionalities of the organic linkers decorating the pores, which are identical in both sets of frameworks. The metal node ($Ca^{2+}$ or $Sr^{2+}$) does not directly participate in the primary guest binding, and its substitution serves only to provide the necessary structural robustness for the diffraction experiment. Thus, by immersing single crystals of **4′** and **5′** in aqueous solutions of perfluorobutanoic acid (PFBA) and perfluorooctanoic acid (PFOA), respectively, we successfully determined the crystal structures of the resulting host-guest adsorbates, **PFBA@4′** and **PFOA@5′**. This analysis, performed at 250 K, allowed for the precise identification of the binding locations and conformations of the guest molecules within the MOF pores (Fig. 4 and S14–S18). Importantly, the frameworks of **4′** and **5′** remained isoreticular upon guest inclusion, showing no significant lattice expansion (Table S1).

In **PFBA@4′**, the primary interaction governing the capture of PFBA within the channels of MOF **4′** is a distinct σ-hole stabilization between the sulfur atom of the L-methionine side chain and an oxygen atom of the PFBA's carboxylate group, with

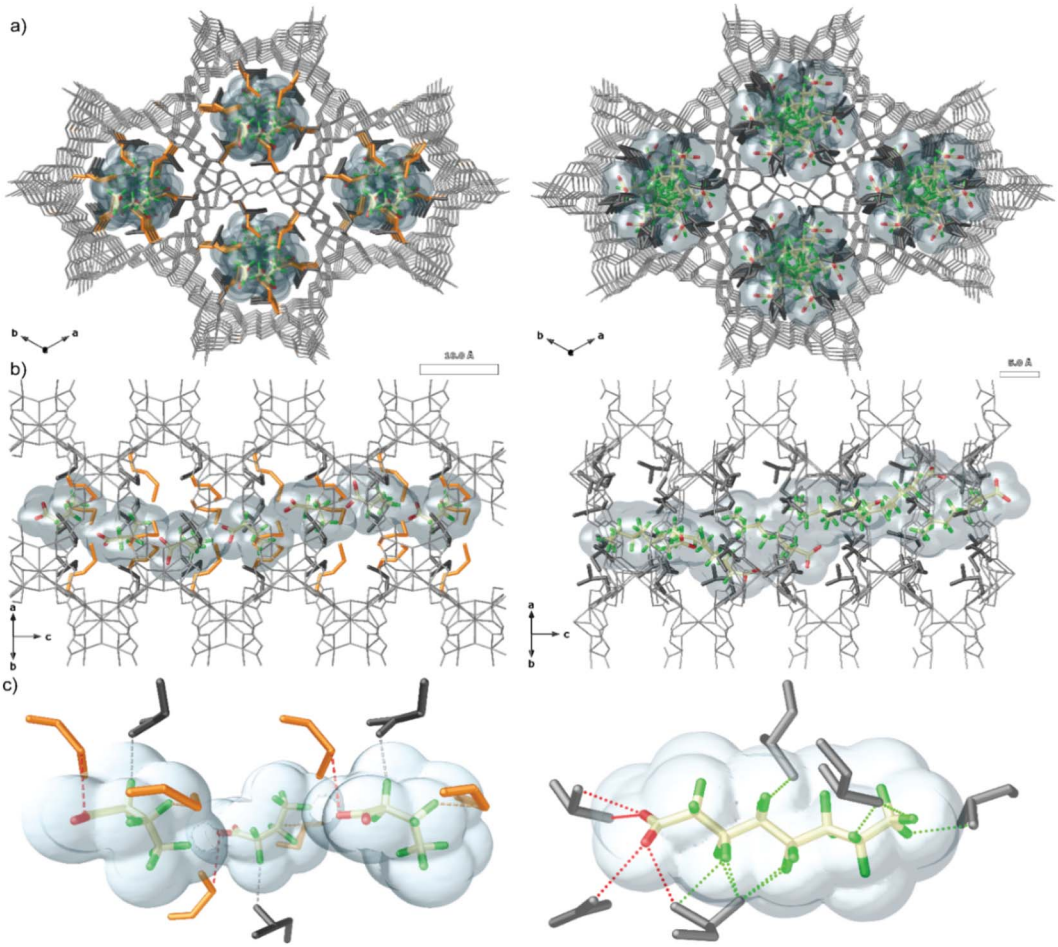


Fig. 4 (a) Perspective view of the 3D open-frameworks of **PFBA@4′** (left) and **PFOA@5′** (right) along the *c* axis. (b) Single channel of **PFBA@4′** (left) and **PFOA@5′** (right) along the *c* direction. (c) Fragment of **PFBA@4′** (left) and **PFOA@5′** (right) emphasizing the interactions of PFBA and PFOA with the framework. Metal atoms and ligands from the network are depicted as grey sticks with the exception of amino acid side chains, which are represented by orange ($-CH_2CH_2SCH_3$) and dark-grey ($-CH_2CH(CH_3)_2$) thick sticks. S atoms are represented with orange spheres. F, C and O atoms from PFBA and PFOA units in **PFBA@4′** and **PFOA@5′**, respectively, are depicted as green, pale yellow and red spheres, respectively. They are highlighted with a blue surface for a better visualization.

 

a measured S···O distance of 3.27 Å (Fig. S14–S16). This effective directional interaction firmly anchors the head of the PFAS molecule. The perfluorinated tail of PFBA is further stabilized by multiple weak C–F···H–C short contacts with the organic linkers of the framework, exhibiting F···H and F···C interatomic distances of 2.33 Å and 2.85 Å, respectively, shorter than the sum of the van der Waals radii (Fig. S14 and S15). These collective interactions precisely orient the PFBA molecule within the MOF's channels, which run along the *c*-axis (Fig. S16).

In the **PFOA@5′** crystal structure, the carboxylate head group of PFOA engages in bifurcated C···O and C···F interactions with the framework, with short distances ranging from 2.82–3.13 Å and 2.35–2.44 Å, respectively (Fig. S17). In addition, a key feature of this system is the role of lattice water molecules, which act as bridges between the guest and the host. These water molecules facilitate C–F···$O_{water}$ halogen bonds (with distances of 3.06 Å and 3.11 Å), further stabilizing the PFOA molecule within the pores (Fig. S18). This network of interactions highlights a cooperative binding mechanism involving both the MOF's functional groups and co-adsorbed water.

In both cases, all those experimental short distances represent weak bonding that should include some significant covalence. Thus, the interactions of the MOF-lining functional groups with PFAS might be considered as a further tuneable parameter together with the hydrophobicity/hydrophilicity of the pores. The encapsulated PFBA and PFOA molecules adopt a predominantly linear conformation, which maximizes the stabilizing halogen bonds along their $C_4$ and $C_8$ tails (Fig. S14 and S17). Crystallographic analysis revealed that each $Cu_2$(-methox/leumox) or $Cu_2$(leumox) dimer binds one PFAS molecule. However, the occupancy was found to be 0.33 PFAS molecules per $Cu_2$ dimer, a likely consequence of the significant kinetic radii of the guest molecules.

The multitude of potential interaction sites led to a statistically disordered arrangement of the guest molecules, as detailed in the SI. This study represents a significant milestone,

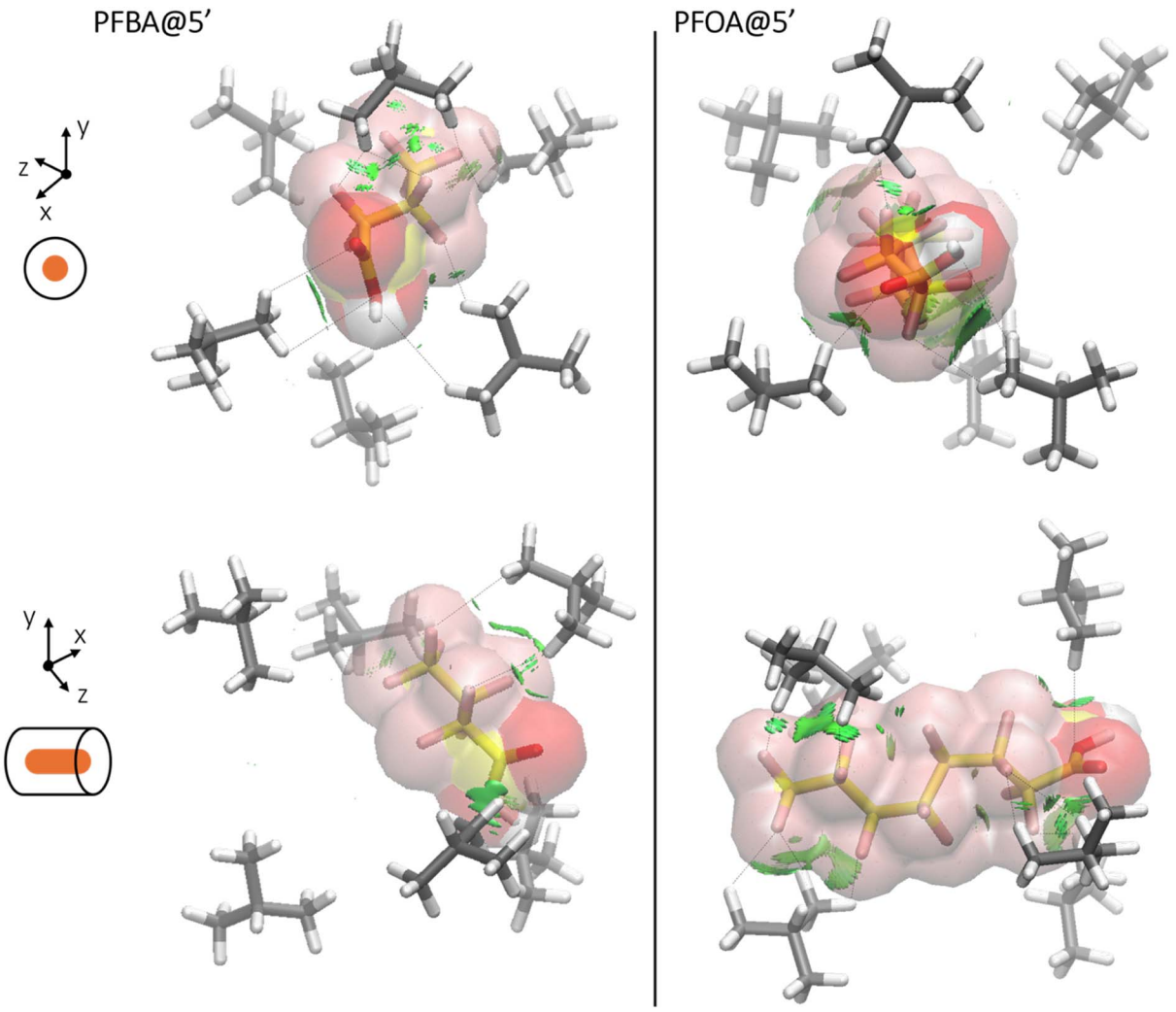


Fig. 5 Top- and side-views of high-layer region of **PFBA@5′** (left) and **PFOA@5′** (right) species, optimized at B3LYP/6-31G(d)|UFF level of theory. C and H atoms of MOF's L-leucine groups are coloured in grey and white, respectively, while C and F atoms of PFBA and PFOA are coloured in yellow and pink, respectively. Host-guest interactions are highlighted by green surfaces.

providing rare direct crystallographic evidence of coordinated PFBA and PFOA within a porous material. These findings unequivocally demonstrate that the strategic incorporation of appropriate chemical functionalities within MOF pores is crucial for achieving the chemisorption and efficient capture of different PFAS molecules. Finally, PXRD patterns **PFBA@4′** (Fig. S19) and **PFOA@5′** (Fig. S20) – performed on samples of both compounds obtained by grinding multiple crystals – confirm the purity and homogeneity of the bulk samples, as they are identical to those theoretical patterns obtained from SCXRD carried out for one single crystal.

### 2.4 Theoretical calculations

Encouraged by the capture performance of MOF **5**, deeper investigation into its recognition of two representative short- and long-chain PFAS such as PFBA and PFOA, was carried out *via* computational approach, taking advantage of the real crystal structure of **PFOA@5′** determined by SCXRD. Thus, starting from the minimal unit of **PFOA@5′** crystallographic structure (Fig. 4), the models of **PFBA@5′** and **PFOA@5′** were built up and geometry-optimized using QM/MM-ONIOM approach (Fig. S21),[75] following a modelling protocol successfully applied in a previous investigation.[76]

In agreement with single-crystal X-ray outcomes, the geometry optimizations of **PFOA@5′** complex reveal that $-CF_2^-$ and $-CF_3$ groups of the considered PFAS lie in the MOF's pore in a linear- staggered conformation (Fig. 5), and, in such binding mode, the organic compound establishes effective interactions with aliphatic $-CH_3$ moieties of L-leucine residues. This is particularly evidenced by the L-leucine group at distances ranging in 2.71–2.94 Å and 2.52–2.85 Å from carboxylic group and C–F respectively (Fig. 5). All these interactions contribute to stabilize the formation of **PFOA@5′**, as confirmed by $-6.7$ kcal mol$^{-1}$ complexation energy and by the plot of short interactions (green surfaces in Fig. 5 and Table S6).

Calculations on **PFBA@5′** nicely revealed that the $C_4$-PFAS can occupy small pockets vicinal to L-leucine groups, to maximize the interactions with the MOF in a linear/staggered conformation of the fluoride-containing groups and, therefore, to stabilize the formation of the complex (see Fig. 5). This possibility would not be available for other MOFs currently presented, which would hold other functions occupying the room, as in the case of L-methionine groups in MOF **4**. This structural feature can explain the enhanced capability of MOF **5** in removing short-chain PFAS. Furthermore, after the geometry-optimization, it can be observed that L-leucine groups resulted at 2.96–3.13 Å and at 2.55–2.91 Å from carboxylic group and C–F respectively (Fig. 5). Although the interaction distances are slightly longer than the respective $C_8$-PFAS, MOF **5** is capable of binding PFBA with a productive complexation energy of $-5.0$ kcal mol$^{-1}$ (Table S6), which well fits with the capture efficiency of *ca* 85% shown in Fig. 2.

Additionally, considering the weak-acid nature of PFAS in water, the affinity of MOF **5** for deprotonated (negatively charged) PFBA and PFOA were evaluated as well. From the calculations, a more negative complexation energy was obtained for both species, with $-9.8$ kcal mol$^{-1}$ and $-11.9$ kcal mol$^{-1}$ for shorter and longer PFAS respectively (Table S6). This result further suggests that MOF **5** can capture the perfluorinated compounds from water solutions, either in neutral or negatively charged forms.

## 3. Conclusions

This study demonstrates the remarkable potential of bio-derived MOFs, particularly MOF **5**, as advanced sorbents for the removal of both long- and short-chain PFAS from water. By tuning the pore functionality through amino acid substitution, we established a clear correlation between increasing hydrophobicity and enhanced PFAS capture performance. MOF **5**, with L-leucine-decorated channels, outperformed its analogues, achieving high removal efficiencies, excellent recyclability, and substantial uptake capacities, even for notoriously difficult short-chain PFAS. Single-crystal X-ray diffraction unveiled key host–guest interactions, including direct coordination to metal centres and hydrophobic interactions within the channels. Thus, the adsorption of short-chain PFAS within hydrophobic MOFs can be conceptualized as a synergistic, two-step process. The dominant driving force arises from the hydrophobic effect, which promotes the exclusion of the fluorinated tail from the aqueous phase and its subsequent insertion into the MOF pores. Concurrently, the hydrophilic head group is anchored to specific functional sites at the pore entrance, representing the molecular recognition step. This cooperative mechanism ensures proper orientation of PFAS molecules within the framework, facilitating efficient packing, enhanced stabilization, and ultimately, high adsorption capacity. These findings underscore the importance of pore environment engineering in MOFs and provide a rational framework for designing future materials aimed at addressing pressing environmental challenges associated with PFAS contamination.

## Conflicts of interest

There are not conflicts of interest to declare.

## Data availability

CCDC 2475573, 2475583 and 2475585 contain the supplementary crystallographic data for this paper.[77a–c]

The data supporting this article have been included as part of the supplementary information (SI). Supplementary information is available. See DOI: **https://doi.org/10.1039/d5ta07539d**.

## Acknowledgements

This work was supported by MCIN/AEI (projects CNS2024-154962, PID2021-125459OB-I00, PID2022-136349OB-I00 and Excellence Unit "Maria de Maeztu" (CEX2024-001467-M)), and by the Ministero dell'Istruzione, dell'Università e della Ricerca (Italy). D. A. gratefully acknowledge financial support from the Italian Ministero dell'Università e della Ricerca (MUR) under

the PRIN 2022 call (Prot. 20224HH9KP, project MUR: 20224HH9KP_002) and Dr Emilia Buchsteiner, Khai Truong and Juergen Graesslin from RIGAKU Europe for data acquisition on single crystal of MOF 4. Thanks are also extended to the "Generalitat Valenciana" (Project PROMETEO/2021/054) and the Ramón y Cajal Program, RYC2019-027940-I (J. F.-S.). This study forms part of the Advanced Materials programme (MFA/2022/048) and was supported by MCIN with funding from European Union NextGenerationEU (PRTR-C17.I1) and by Generalitat Valenciana.

## Notes and references

1 R. C. Buck, J. Franklin, U. Berger, J. M. Conder, I. T. Cousins, P. de Voogt, A. A. Jensen, K. Kannan, S. A. Mabury and S. P. J. van Leeuwen, *Integr. Environ. Assess. Manage.*, 2011, **7**, 513–541.
2 T. Teymourian, T. Teymoorian, E. Kowsari and S. Ramakrishna, *Res. Chem. Intermed.*, 2021, **47**, 4879–4914.
3 C. Beans, *Proc. Natl. Acad. Sci. U. S. A.*, 2021, **118**, e2105018118.
4 H. Brunn, G. Arnold, W. Körner, G. Rippen, K. G. Steinhäuser and I. Valentin, *Environ. Sci. Eur.*, 2023, **35**, 20.
5 L. G. T. Gaines, *Am. J. Ind. Med.*, 2023, **66**, 353–378.
6 J. L. Guelfo, P. L. Ferguson, J. Beck, M. Chernick, A. Doria-Manzur, P. W. Faught, T. Flug, E. P. Gray, N. Jayasundara, D. R. U. Knappe, A. S. Joyce, P. Meng and M. Shojaei, *Nat. Commun.*, 2024, **15**, 5548.
7 F. Pérez, M. Nadal, A. Navarro-Ortega, F. Fàbrega, J. L. Domingo, D. Barceló and M. Farré, *Environ. Int.*, 2013, **59**, 354–362.
8 R. Ghisi, T. Vamerali and S. Manzetti, *Environ. Res.*, 2019, **169**, 326–341.
9 T. Groffen, E. Prinsen, O.-A. Devos Stoffels, L. Maas, P. Vincke, R. Lasters, M. Eens and L. Bervoets, *Environ. Sci. Pollut. Res.*, 2022, **30**, 23820–23835.
10 E. M. Sunderland, X. C. Hu, C. Dassuncao, A. K. Tokranov, C. C. Wagner and J. G. Allen, *J. Exposure Sci. Environ. Epidemiol.*, 2019, **29**, 131–147.
11 N. M. Brennan, A. T. Evans, M. K. Fritz, S. A. Peak and H. E. von Holst, *Int. J. Environ. Res. Public Health*, 2021, **18**, 10900.
12 E. Comission, **https://eur-lex.europa.eu/legal-content/ES/ALL/?uri=CELEX:52024XC04910**.
13 R. Amen, A. Ibrahim, W. Shafqat and E. B. Hassan, *Sustainability*, 2023, **15**, 16173.
14 J. N. Meegoda, B. Bezerra de Souza, M. M. Casarini and J. A. Kewalramani, *Int. J. Environ. Res. Public Health*, 2022, **19**, 16397.
15 N. Yamashita, E. Yamazaki, S. Taniyasu, N. Hanari and L. W. Y. Yeung, *Chemosphere*, 2024, **364**, 143073.
16 C. C. Murray, R. E. Marshall, C. J. Liu, H. Vatankhah and C. L. Bellona, *J. Water Process Eng.*, 2021, **44**, 102342.
17 T. F. Mastropietro, R. Bruno, E. Pardo and D. Armentano, *Dalton Trans.*, 2021, **50**, 5398–5410.
18 M. Riegel, B. Haist-Gulde and F. Sacher, *Environ. Sci. Eur.*, 2023, **35**, 12.
19 D. Saha, S. Khan and S. E. Van Bramer, *J. Environ. Chem. Eng.*, 2021, **9**, 106665.
20 P. McCleaf, S. Englund, A. Östlund, K. Lindegren, K. Wiberg and L. Ahrens, *Water Res.*, 2017, **120**, 77–87.
21 J. B. Burkhardt, N. Burns, D. Mobley, J. G. Pressman, M. L. Magnuson and T. F. Speth, *J. Environ. Eng.*, 2022, **148**, 1–25.
22 F. Li, J. Duan, S. Tian, H. Ji, Y. Zhu, Z. Wei and D. Zhao, *Chem. Eng. J.*, 2020, **380**, 122506.
23 Y. Nakazawa, K. Kosaka, N. Yoshida, M. Asami and Y. Matsui, *Water Res.*, 2023, **245**, 120559.
24 H. Furukawa, K. E. Cordova, M. O'Keeffe and O. M. Yaghi, *Science*, 2013, **341**, 974.
25 H.-C. "Joe" Zhou and S. Kitagawa, *Chem. Soc. Rev.*, 2014, **43**, 5415–5418.
26 G. Maurin, C. Serre, A. Cooper and G. Férey, *Chem. Soc. Rev.*, 2017, **46**, 3104–3107.
27 S. Kitagawa and R. Matsuda, *Coord. Chem. Rev.*, 2007, **251**, 2490–2509.
28 X. Zhang, B. Wang, A. Alsalme, S. Xiang, Z. Zhang and B. Chen, *Coord. Chem. Rev.*, 2020, **423**, 213507.
29 M. Viciano-Chumillas, X. Liu, A. Leyva-Pérez, D. Armentano, J. Ferrando-Soria and E. Pardo, *Coord. Chem. Rev.*, 2022, **451**, 214273.
30 M. Mon, R. Bruno, E. Tiburcio, M. Viciano-Chumillas, L. H. G. Kalinke, J. Ferrando-Soria, D. Armentano and E. Pardo, *J. Am. Chem. Soc.*, 2019, **141**, 13601–13609.
31 R. Freund, O. Zaremba, G. Arnauts, R. Ameloot, G. Skorupskii, M. Dincă, A. Bavykina, J. Gascon, A. Ejsmont, J. Goscianska, M. Kalmutzki, U. Lächelt, E. Ploetz, C. S. Diercks and S. Wuttke, *Angew. Chem., Int. Ed.*, 2021, **60**, 23975–24001.
32 A. Bavykina, N. Kolobov, I. S. Khan, J. A. Bau, A. Ramirez and J. Gascon, *Chem. Rev.*, 2020, **120**, 8468–8535.
33 P. Escamilla, W. D. Guerra, A. Leyva-Pérez, D. Armentano, J. Ferrando-Soria and E. Pardo, *Chem. Commun.*, 2023, **59**, 836–851.
34 M. Viciano-Chumillas, M. Mon, J. Ferrando-Soria, A. Corma, A. Leyva-Pérez, D. Armentano and E. Pardo, *Acc. Chem. Res.*, 2020, **53**, 520–531.
35 M. Giménez-Marqués, T. Hidalgo, C. Serre and P. Horcajada, *Coord. Chem. Rev.*, 2016, **307**, 342–360.
36 S. Rojas and P. Horcajada, *Chem. Rev.*, 2020, **120**, 8378–8415.
37 M. Mon, R. Bruno, J. Ferrando-Soria, D. Armentano and E. Pardo, *J. Mater. Chem. A*, 2018, **6**, 4912–4947.
38 H. Li, A. L. Junker, J. Wen, L. Ahrens, M. Sillanpää, J. Tian, F. Cui, L. Vergeynst and Z. Wei, *Chem.–Eng. J.*, 2023, **452**, 139202.
39 M. Mon, R. Bruno, J. Ferrando-Soria, L. Bartella, L. Di Donna, M. Talia, R. Lappano, M. Maggiolini, D. Armentano and E. Pardo, *Mater. Horiz.*, 2018, **5**, 683–690.
40 R. J. Young, M. T. Huxley, E. Pardo, N. R. Champness, C. J. Sumby and C. J. Doonan, *Chem. Sci.*, 2020, **11**, 4031–4050.
41 R. Li, N. N. Adarsh, H. Lu and M. Wriedt, *Matter*, 2022, **5**, 3161–3193.

42 L. I. FitzGerald, J. F. Olorunyomi, R. Singh and C. M. Doherty, *ChemSusChem*, 2022, **15**, e202201136.
43 K. Liu, S. Zhang, X. Hu, K. Zhang, A. Roy and G. Yu, *Environ. Sci. Technol.*, 2015, **49**, 8657–8665.
44 M.-J. Chen, A.-C. Yang, N.-H. Wang, H.-C. Chiu, Y.-L. Li, D.-Y. Kang and S.-L. Lo, *Microporous Mesoporous Mater.*, 2016, **236**, 202–210.
45 R. Li, S. Alomari, T. Islamoglu, O. K. Farha, S. Fernando, S. M. Thagard, T. M. Holsen and M. Wriedt, *Environ. Sci. Technol.*, 2021, **55**, 15162–15171.
46 R. Sharma, Z. Zhou, T. Themelis, T. R. C. Van Assche, S. Eeltink and J. F. M. Denayer, *Langmuir*, 2023, **39**, 3341–3349.
47 J. Pala, T. Le, M. Kasula and M. Rabbani Esfahani, *Sep. Purif. Technol.*, 2023, **309**, 123025.
48 E. Loukopoulos, S. Marugán-Benito, D. Raptis, E. Tylianakis, G. E. Froudakis, A. Mavrandonakis and A. E. Platero-Prats, *Adv. Funct. Mater.*, 2024, **34**, 1–8.
49 R.-R. Liang, S. Xu, Z. Han, Y. Yang, K.-Y. Wang, Z. Huang, J. Rushlow, P. Cai, P. Samorì and H.-C. Zhou, *J. Am. Chem. Soc.*, 2024, **146**, 9811–9818.
50 S. Li, J. Ma, J. Cheng, G. Wu, S. Wang, C. Huang, J. Li and L. Chen, *Langmuir*, 2024, **40**, 2815–2829.
51 K. Zhang, P. Cheng, Y. Liu and S. Xia, *Water Res.*, 2024, **265**, 122276.
52 N. Ilić, K. Tan, F. Mayr, S. Hou, B. M. Aumeier, E. M. C. Morales, U. Hübner, J. Cookman, A. Schneemann, A. Gagliardi, J. E. Drewes, R. A. Fischer and S. Mukherjee, *Adv. Mater.*, 2025, **37**, 1–14.
53 Y. Li, Z. Yang, Y. Wang, Z. Bai, T. Zheng, X. Dai, S. Liu, D. Gui, W. Liu, M. Chen, L. Chen, J. Diwu, L. Zhu, R. Zhou, Z. Chai, T. E. Albrecht-Schmitt and S. Wang, *Nat. Commun.*, 2017, **8**, 1354.
54 K. Sini, D. Bourgeois, M. Idouhar, M. Carboni and D. Meyer, *New J. Chem.*, 2018, **42**, 17889–17894.
55 B.-M. Jun, H. S. Hwang, J. Heo, J. Han, M. Jang, J. Sohn, C. M. Park and Y. Yoon, *J. Ind. Eng. Chem.*, 2019, **79**, 345–352.
56 C. A. Clark, K. N. Heck, C. D. Powell and M. S. Wong, *ACS Sustainable Chem. Eng.*, 2019, **7**, 6619–6628.
57 D. Barpaga, J. Zheng, K. S. Han, J. A. Soltis, V. Shutthanandan, S. Basuray, B. P. McGrail, S. Chatterjee and R. K. Motkuri, *Inorg. Chem.*, 2019, **58**, 8339–8346.
58 Z. Guo, J. Liu, Y. Li, J. A. McDonald, M. Y. Bin Zulkifli, S. J. Khan, L. Xie, Z. Gu, B. Kong and K. Liang, *Chem. Commun.*, 2020, **56**, 14837–14840.
59 Y. Yang, Z. Zheng, W. Ji, J. Xu and X. Zhang, *J. Hazard. Mater.*, 2020, **395**, 122686.
60 R. Li, S. Alomari, R. Stanton, M. C. Wasson, T. Islamoglu, O. K. Farha, T. M. Holsen, S. M. Thagard, D. J. Trivedi and M. Wriedt, *Chem. Mater.*, 2021, **33**, 3276–3285.
61 Y. Wen, P. Zhang, V. K. Sharma, X. Ma and H.-C. Zhou, *Cell Rep. Phys. Sci.*, 2021, **2**, 100348.
62 M. Mon, J. Ferrando-Soria, T. Grancha, F. R. Fortea-Pérez, J. Gascon, A. Leyva-Pérez, D. Armentano and E. Pardo, *J. Am. Chem. Soc.*, 2016, **138**, 7864–7867.
63 M. Mon, A. Pascual-Álvarez, T. Grancha, J. Cano, J. Ferrando-Soria, F. Lloret, J. Gascon, J. Pasán, D. Armentano and E. Pardo, *Chem. –Eur. J.*, 2016, **22**, 539–545.
64 A. Abhervé, T. Grancha, J. Ferrando-Soria, M. Clemente-León, E. Coronado, J. C. Waerenborgh, F. Lloret and E. Pardo, *Chem. Commun.*, 2016, **52**, 7360–7363.
65 R. Bruno, M. Mon, P. Escamilla, J. Ferrando-Soria, E. Esposito, A. Fuoco, M. Monteleone, J. C. Jansen, R. Elliani, A. Tagarelli, D. Armentano and E. Pardo, *Adv. Funct. Mater.*, 2021, **31**, 2008499.
66 C. Negro, H. Martínez Pérez-Cejuela, E. F. Simó-Alfonso, J. M. Herrero-Martínez, R. Bruno, D. Armentano, J. Ferrando-Soria and E. Pardo, *ACS Appl. Mater. Interfaces*, 2021, **13**, 28424–28432.
67 C. Negro, H. Martínez Pérez-Cejuela, E. F. Simó-Alfonso, W. Iqbal, J. M. Herrero-Martínez, D. Armentano, J. Ferrando-Soria and E. Pardo, *ACS Appl. Mater. Interfaces*, 2023, **15**, 3069–3076.
68 C. Negro, P. Escamilla, R. Bruno, J. Ferrando-Soria, D. Armentano and E. Pardo, *Chem.–Eur. J.*, 2022, **28**, e202200034.
69 T. Grancha, P. Garcia-Atienza, S. Armenta, J. M. Herrero-Martínez, R. M. Percoco, D. Armentano, J. Ferrando-Soria and E. Pardo, *J. Mater. Chem. A*, 2025, **13**, 24473–24482.
70 Y. Yan, E. J. Carrington, R. Pétuya, G. F. S. Whitehead, A. Verma, R. K. Hylton, C. C. Tang, N. G. Berry, G. R. Darling, M. S. Dyer, D. Antypov, A. P. Katsoulidis and M. J. Rosseinsky, *J. Am. Chem. Soc.*, 2020, **142**, 14903–14913.
71 M. Mon, R. Bruno, E. Tiburcio, P.-E. Casteran, J. Ferrando-Soria, D. Armentano and E. Pardo, *Chem.–Eur. J.*, 2018, **24**, 17712–17718.
72 T. Grancha, M. Mon, J. Ferrando-Soria, J. Gascon, B. Seoane, E. V. Ramos-Fernandez, D. Armentano and E. Pardo, *J. Mater. Chem. A*, 2017, **5**, 11032–11039.
73 M. F. De Lange, T. J. H. Vlugt, J. Gascon and F. Kapteijn, *Microporous Mesoporous Mater.*, 2014, **200**, 199–215.
74 E. R. Pezoulas, B. Tajdini, Y. Ko, A. A. Uliana, R. Giovine, H. Furukawa, H. Vatankhah, J. Börgel, K. C. Kim, C. Bellona and J. R. Long, *J. Am. Chem. Soc.*, 2025, **147**, 21832–21843.
75 L. W. Chung, W. M. C. Sameera, R. Ramozzi, A. J. Page, M. Hatanaka, G. P. Petrova, T. V. Harris, X. Li, Z. Ke, F. Liu, H.-B. Li, L. Ding and K. Morokuma, *Chem. Rev.*, 2015, **115**, 5678–5796.
76 M. Mon, R. Bruno, S. Sanz-Navarro, C. Negro, J. Ferrando-Soria, L. Bartella, L. Di Donna, M. Prejanò, T. Marino, A. Leyva-Pérez, D. Armentano and E. Pardo, *Nat. Commun.*, 2020, **11**, 3080.
77 (*a*) CCDC 2475573: Experimental Crystal Structure Determination, 2025, DOI: **10.5517/ccdc.csd.cc2p3162**; (*b*) CCDC 2475583: Experimental Crystal Structure Determination, 2025, DOI: **10.5517/ccdc.csd.cc2p31jd**; (*c*) CCDC 2475585: Experimental Crystal Structure Determination, 2025, DOI: **10.5517/ccdc.csd.cc2p31lg**.

 